Probing the Internal Structure of High-Performance Fibers by On-Axis Scanning Diffractometry

Richard J. Davies,* Manfred Burghammer, and Christian Riekel

European Synchrotron Radiation Facility, 6 rue Jules Horowitz, BP220, Grenoble Cedex 48043, France

Received September 5, 2006; Revised Manuscript Received April 20, 2007

ABSTRACT: Many high-performance fibers exhibit radial anisotropy or a skin−core morphology. This influences their mechanical properties, affects the interfacial characteristics of composite systems, and needs consideration when interpreting results collected using localized probing techniques. This study reports on the direct observation of crystallographic texture and rotational disorder within a single high-performance fiber. This is possible using a microfocused X-ray beam to obtain diffraction patterns along the fiber axis. This enables radial anisotropy to be investigated without the need for modeling. The results indicate that the high-performance fiber studied exhibits a rotationally disordered skin and core, with preferred orientation extending throughout the fiber. Variations in the skin's width and core position are taken as evidence of heterogeneous coagulation. The experimental results can be explained by a fiber formation model in which oriented crystalline domains extend inward, toward the fiber center. These results allow a number of findings from previous model-based studies to be validated.

1. Introduction

The internal morphology of high-performance fibers is an important, yet often neglected subject. This is surprising considering that radial anisotropy, or so-called "skin−core" morphology, is known to influence mechanical properties[1−3] and can alter the interfacial characteristics of composite systems. This subject's relative neglect can be attributed to difficulties in the assessment of microstructural variations in such small sample volumes (typically $<15\ \mu$m). For example, while optical microscopy is readily accessible, it is only of limited use on these length scales. Many microstructural features lie well beyond its resolving limit. Most studies have therefore employed atomic or interfacial force microscopy (AFM and IFM),[2,3] scanning electron microscopy (SEM), or electron diffraction (ED) techniques.[4,5] However, these methods are also limited by the requirement of using only thinly sectioned and/or conductively coated samples. This risks the introduction of artificial texture and other local damage.[6] Such artifacts can compromise microstructural studies as they tend to rely upon extrapolating highly localized information to bulk length scales. In addition, ED studies can be technically challenging for soft-condensed matter because of its susceptibility to beam damage.[7]

As an alternative, several studies have successfully employed microfocus X-ray diffraction (μXRD) to study skin−core morphology and other microscopic structural features in single fibers.[8−12] This requires an X-ray beam which is considerably smaller than a single fiber's diameter. Such beams, having micrometer and sub-micrometer dimensions, are routinely available at specialist synchrotron radiation (SR) facility beamlines.[13] μXRD offers a unique combination of advantages for studying the internal morphology of single fibers. It can access structural information spanning a range of different length scales, without the need for sample sectioning and while causing negligible beam damage to most high-performance polymers. For such studies, beam size is a critical parameter. It dictates the spatial resolution for scanning experiments and defines the degree of morphological averaging at each scan position.[12] Recent advances in beamline instrumentation have resulted in a choice of focusing optics which provide beam dimensions of 500 nm or less.[10,11,13] To put this in perspective, only a few years ago most μXRD studies employed X-ray beams having diameters greater than 3 μm.[8,9,14] Meanwhile, there have been similar advances in detector technology. Consequently, two-dimensional (2D) raster scans can now be performed at higher spatial resolutions and covering larger areas. In addition, the development of highly automated data treatment software now allows thousands of diffraction patterns to be analyzed in a relatively short time frame.[15,16] Because of the combination of these developments, μXRD has now become a more applicable and practical tool than ever before.

Virtually all preceding μXRD studies of single fibers have been carried out in a "standard" fiber diffraction geometry (with the fiber perpendicular to the incoming beam). In this geometry, radial anisotropy can be investigated by comparing diffraction patterns collected at different positions across the fiber's width. Those diffraction patterns collected at the very edge of the fiber represent the morphology of the skin region. Meanwhile, those patterns collected at the fiber's center contain both a skin and core contribution (from which the skin can either be subtracted or neglected, depending upon its thickness). In this way it is possible to probe skin−core morphological variations within a single fiber. However, a considerable limitation of this geometry is the lack of information regarding a scattering element's position along the beam axis. Thus, variations which arise between diffraction patterns can only be related in general terms to the fiber's internal structure. Modeling, although complicated, can provide a way of overcoming this limitation. However, it requires many assumptions to "project" the information obtained in transmission onto a model of the fiber's cross section. As many of these assumptions have yet to be experimentally validated, it is difficult to impartially assess the accuracy of such models.

This study reports on a μXRD experiment of a single high-performance fiber carried out using a 500 nm X-ray beam. Unlike previous studies,[8−12] this experiment employs a novel on-axis geometry coupled with high-resolution 2D scanning diffractometry. This technique allows the fiber's cross-sectional microstructure to be spatially resolved directly, eliminating the

* Corresponding author. E-mail: rdavies@esrf.fr.

10.1021/ma062049g CCC: $37.00
Published on Web 06/15/2007

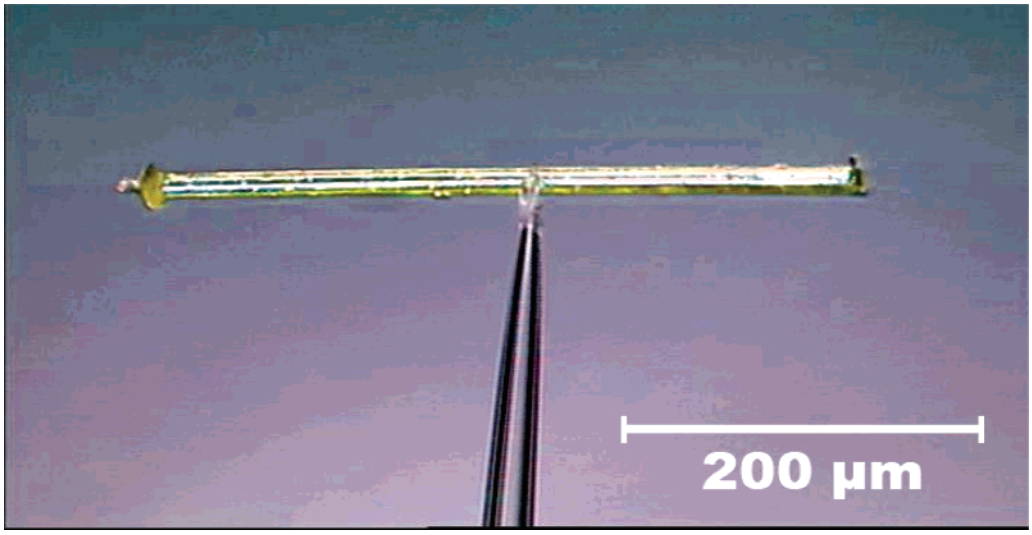

Figure 1. Micrograph from the ID13 beamline microscope (50× objective) showing a 400 μm length of PBO fiber attached to the end of a pulled capillary.

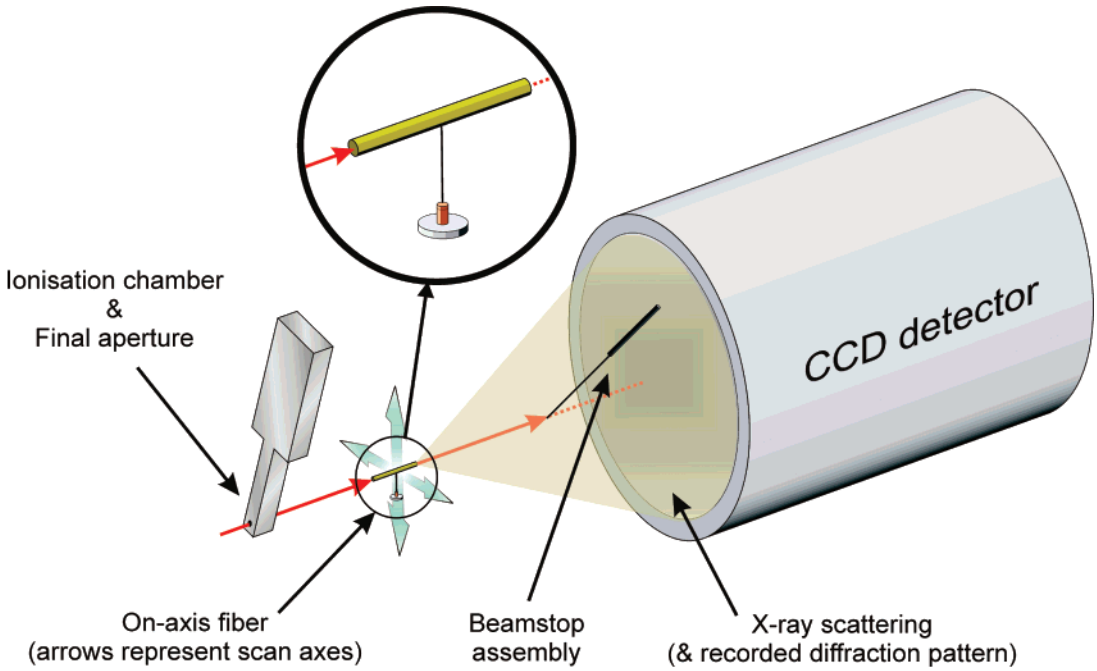

Figure 2. Annotated schematic showing experimental geometry for on-axis diffraction (note that diagram contents are not shown to scale).

need for modeling. This approach provides a new level of insight into skin−core morphology and crystallographic texturing within single high-performance fibers. In addition, it allows the accuracy of several existing fiber morphology models, which have yet to be experimentally validated, to be assessed. In combination with existing information about the fiber manufacturing process, the origins of various morphological features can also be inferred.

2. Experimental Section

2.1. Materials. The high-performance fiber poly(*p*-phenylene benzobisoxazole) (or PBO) is investigated in this study. This fiber type is manufactured by Toyobo (Japan) under the trade name Zylon. PBO belongs to a class of materials known as rigid rods due to their common structure of highly extended, highly oriented molecular chains. This, in combination with a high degree of crystallinity, is responsible for the fiber's remarkable mechanical properties.[17] PBO is produced using a dry-jet wet-spinning method in which the fiber is extruded from the nematic dope, through an air gap, and coagulated in an aqueous solution. After a drying process, preparation of the as-spun (AS) variety of PBO is complete. This is the variety used in this present study and has been selected due to its more pronounced skin−core morphology compared to the heat-treated high-modulus fiber (HM).[14] Its diameter is reported as 12.3 μm.[18]

Preparation of a PBO sample for μXRD involved cutting short lengths of PBO fibers (each ∼400 μm in length) from a bundle containing several hundred using a razor blade. A microscope was used to select the least damaged fiber segment. This was then attached to the end of a pulled capillary (perpendicularly), using a small amount of paraffin wax. The capillary holding the fiber was mounted on a magnetic base compatible with the beamline microgoniometer. The use of a 400 μm length of fiber was carefully considered. On one hand, it is necessary to use a relatively long length to minimize the scattering contribution from the damaged ends. However, on the other hand, the length should not be so great that the fiber bends under its own weight. For PBO, which is a so-called rigid rod, 400 μm was found to be a good compromise between these two considerations. A micrograph of the PBO fiber length prepared for this study is shown in Figure 1.

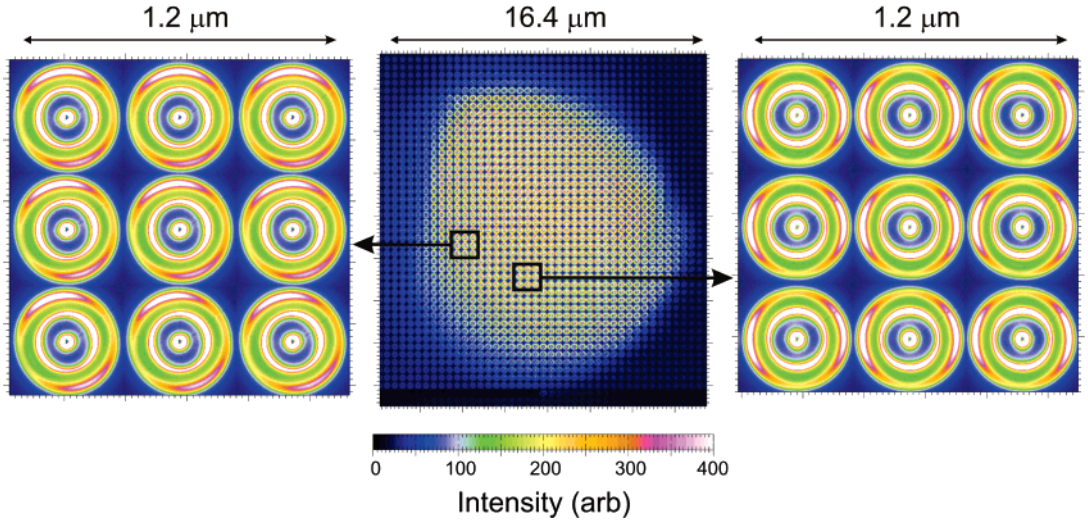

Figure 3. A composite image reflecting the real-space scan position where each diffraction pattern was obtained. Two regions are shown in greater detail to illustrate the appearance of individual patterns within the context of the larger scan region.

2.2. Scanning X-ray Diffractometry. Scanning μXRD was carried out at ID13, the microfocus beamline of the European Synchrotron Radiation Facility (ESRF). The beamline was configured with a monochromatic beam ($\lambda \approx 0.098$ nm). The beam was focused using a pair of crossed, short focal length Kirkpatrick Baez mirrors. This provided a beam spot size at the focal position of approximately 500×500 nm^2. The addition of a final aperture incorporating an ionization chamber enabled the exposure to be adjusted to account for fluctuations in beam brilliance. Data collection was performed using a 16-bit MARCCD detector with an average pixel size of 79×79 μm^2. Figure 2 shows a schematic of the experimental geometry used for data collection in which the aforementioned beamline elements are annotated.

The capillary (supporting the fiber) was mounted at the X-ray beam's focal position, on two perpendicular microgoniometers and a rotation stage. Initially the fiber was aligned visually to the X-ray beam axis using the beamline's sample environment microscope (which is mounted on-axis with the X-ray beam). The fiber's alignment was then fine-tuned by assessing diffraction pattern symmetry. An iterative alignment process allowed the fiber to be aligned to within 0.25° from the beam axis (estimated). For data collection, diffraction patterns were generated using a 2D raster scan to cover the region containing the fiber. This was 24 μm along both axes with a 400 nm step size between adjacent patterns. The resulting "mesh" therefore contained 3721 individual diffraction patterns, each collected using an exposure time of ~1 s (although individual times varied slightly with fluctuations in beam brilliance). A composite image showing the central region of each diffraction pattern obtained at each scan position is shown in Figure 3. The outline of the fiber is clearly visible from the variation in scattering intensity. Two regions, each containing nine individual patterns, are shown in Figure 3 in greater detail. This illustrates the appearance of individual patterns within the context of the larger scan region. Note that although the scan range was 24 μm along both axes, only the scan region containing the fiber is shown in Figure 3, in common with all others figures presented in this study.

2.3. Analysis. Diffraction pattern analysis and visualization were carried out using the Fit2D software application[19] in combination with specialist data reduction and automated batch-analysis software.[15,16] Each diffraction pattern was background subtracted and radially integrated to produce azimuthal scattering profiles covering a 360° azimuthal range. These were generated around the two radial positions containing the greatest scattering contributions. The integration regions and the resulting azimuthal profiles are shown in Figure 4 for a typical diffraction pattern collected on-axis. The fully automatic, batch-processing algorithm used for analysis includes several specialized features for fitting azimuthal diffraction data.[16] These include accommodating the wraparound and asymmetric nature of azimuthal profiles, the use of a common half-width at half-maximum (HWHM) parameter across both hemispheres, and spread-estimate fitting over the entire 360° azimuthal range. Figure 4 shows an example of two Gaussian functions fitted to each of the azimuthal profiles generated from a typical on-axis diffraction pattern. The excellent correlation between the fitted function and experimental data demonstrates model applicability.

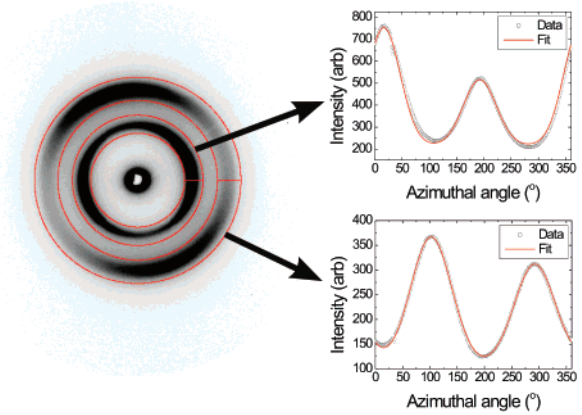

Figure 4. Demonstration of the integration regions used for generating azimuthal scattering profiles from a typical PBO on-axis diffraction pattern. The final function fits are also shown, as used for parameter determination.

3. Results

Several on-axis diffraction patterns have already been shown in Figures 3 and 4. In each case they are characterized by two strong "rings", both of which are azimuthally anisotropic. These scattering contributions arise from crystal planes which have an average alignment that is close to parallel with the fiber axis. They would therefore appear as "equatorial" reflections in the standard fiber diffraction geometry (with the fiber perpendicular to the incoming beam). The reflection closest to the beam center can be indexed as the 200 reflection while the second "ring" contains a contribution from both the 010 and $\bar{2}10$ reflections.[20] These latter reflections appear indistinguishable due to their close proximity and rather diffuse radial profile on the detector.

The on-axis scattering contributions in Figures 3 and 4 can be interpreted using the Ewald construction. Given an ideal fiber orientation, all PBO *hk*0 reciprocal lattice points will lie on a plane tangential to the Ewald sphere's surface when [001] is along the beam axis. Diffraction from (*hk*0) crystal planes is

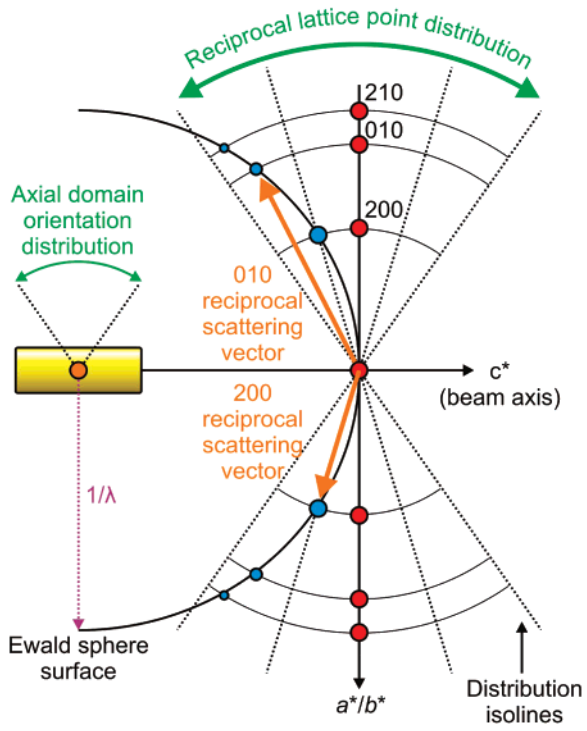

Figure 5. Schematic representation of the Ewald construction corresponding to the on-axis diffraction geometry for PBO.

therefore precluded as no point on this plane will intersect with the surface of the Ewald sphere. On this basis, the diffraction patterns in Figures 3 and 4 demonstrate a distribution in PBO crystalline domain orientation with respect to the beam axis. Such a distribution in real space corresponds to an identical distribution within the Ewald construction (replicated as a rotation of the reciprocal lattice about its origin). Although this is sufficient for 200, 010, and $\bar{2}10$ reciprocal lattice points to intersect with the surface of the Ewald sphere during on-axis diffraction, PBO nevertheless has a high degree of axial domain orientation. As such, the observed reflection intensities will exhibit a strong dependence upon reciprocal scattering vector length since this length dictates the distance from the mean *hk*0 lattice point to the Ewald sphere's surface. As this distance increases, the observed reflection intensity will decrease as the deviation from the distribution mean corresponds to fewer diffracting crystalline domains. Consequently, the outer "ring" in Figures 3 and 4 is dominated by scattering from (010) crystal planes rather than ($\bar{2}10$) (due to its longer reciprocal scattering vector). To clarify this, Figure 5 shows a schematic of the Ewald construction representing the on-axis diffraction of PBO.

The azimuthal anisotropy in Figures 3 and 4 reflects a preferred orientation of crystal planes within the fiber. This common crystal plane orientation must exist over length scales that are greater than the beam diameter for these features to be so clearly visible. This demonstrates the value of utilizing submicrometer X-ray beams as a larger beam (>10 μm) would be unable to resolve any preferred orientation whatsoever. An isotropic small-angle scattering contribution is also visible around the beamstop in Figures 3 and 4. This corresponds to scattering from the fiber's capillary-like microvoid and fibrillar structure.[21]

3.1. Crystallographic Texture. From each *hk*0 reflection within each diffraction pattern, an azimuthal position of maximum scattering intensity can be deduced by model fitting. This azimuthal angle will be perpendicular (in the detector plane) to the mean orientation of (*hk*0) crystal planes. Consequently,

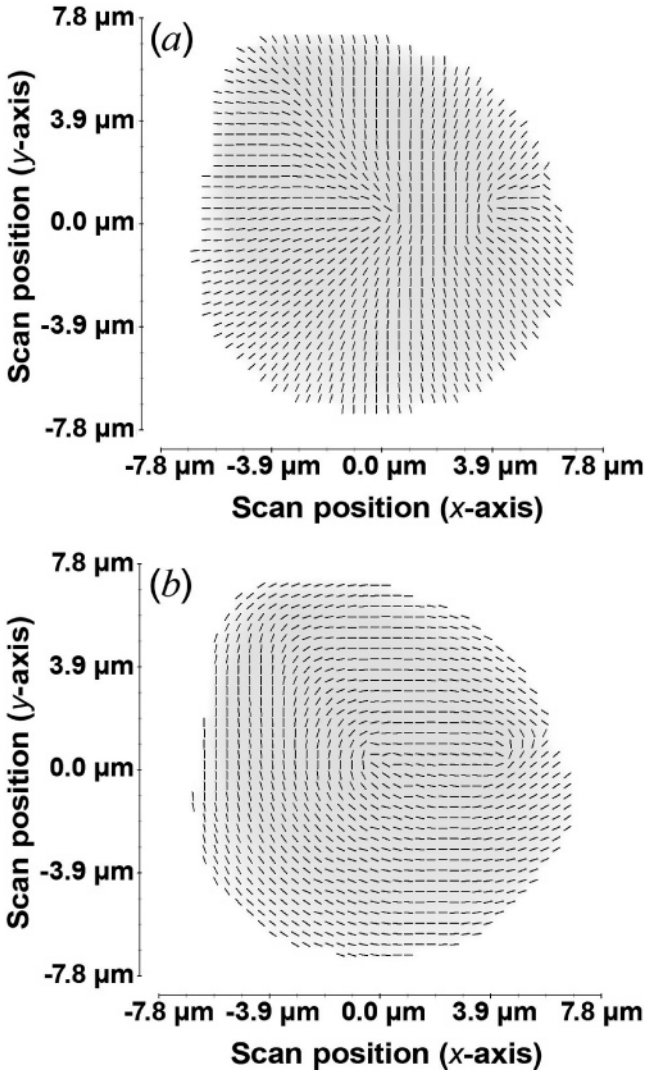

Figure 6. Vector plots showing the mean azimuthal orientation of (a) (010)/($\bar{2}10$) and (b) (200) crystal planes at each scan position within the fiber cross section.

by calculating this azimuthal maximum for each scan position, it is possible to deduce mean crystal plane orientation and then relate this to the fiber's cross-sectional geometry. These relationships are shown in Figure 6 for the (010)/($\bar{2}10$) and (200) crystal planes. Fixed length vectors are used to indicate azimuthal orientation in the detector plane, as derived from each pattern in the scan.

Figure 6 shows that, on average, (010)/($\bar{2}10$) crystal planes are radially oriented with respect to the fiber axis while (200) crystal planes are aligned azimuthally. This therefore indicates a fiber-scale crystallographic texture in which the *a*-axis is oriented radially. It is important to note that this only refers to the *average* orientation of all contributing crystalline domains within the illuminated gauge volume. Therefore, it does not necessarily mean that the *a*-axis is strictly radial for individual domains given an idealized crystallographic texture (i.e., without the influence of domain misorientation). For example, it is also possible that the *a*-axis is systematically offset from the radial direction by a relatively small angle. This offset, when coupled with axial symmetry and convoluted with the distribution in crystalline domain orientation, may still result in the largest fraction of those domains being aligned with their *a*-axes radially.

This effect can be observed directly in the relationship between the (200) and (010)/($\bar{2}10$) crystal plane orientations.

According to the PBO unit cell, the internal angle (γ) between the (200) and (010) crystal planes is 101.3°.[20] Assuming a given unit cell direction is always strictly radial, the oblique angle γ must result in at least one of the scattering profiles being azimuthally split. For example, if [010] is radially aligned about the fiber axis, [100] will appear perpendicular to [010] on the detector azimuth and as a doublet having an azimuthal split of ±11.3°. However, the azimuthal profiles in Figure 4 show no azimuthal split in either series. This demonstrates how domain misorientation averages out crystallographic texture such that only mean orientations can be determined. Thus, Figure 6 only demonstrates that the *a*-axis is, on average, radially aligned. This does not necessarily mean that the *a*-axis is strictly radial within the idealized structure of PBO.

The crystallographic texture shown in Figure 6 has been reported previously from highly localized electron diffraction studies.[17,22] More recently, X-ray diffraction has also inferred this morphology[11] which is shared by the poly(*p*-phenylene phthalamide) (or PPTA) high-performance fiber.[9,10] This type of preferred orientation can be described using an idealized model of radial fibrillar texture (RFT).[9−11] This reflects the fact that, although the fiber's structure consists of a fibrillar network, crystalline domains within fibrils follow a macroscopic orientation over fiber—rather than fibrillar—length scales. The idealized RFT model relies heavily upon assumptions of fiber symmetry and the extrapolation of single, highly localized measurements to represent bulk microstructure. The fact that Figure 6 confirms the existence of RFT over a fiber length scale is significant. This validates the RFT model's application to a number of different fiber types, including PBO and PPTA. This has hitherto only been inferred indirectly.

While this study demonstrates the existence of preferred crystallographic orientation corresponding to the RFT model, this is not the first time that radial structures have been directly observed over fiber length scales. Hagege et al. employed optical and dark-field electron microscopy to study ultrathin PPTA fiber cross sections.[23,24] Radial bands appearing on the dark-field image were interpreted as a pleated-sheet microstructure, with individual 15 nm crystallites also visible.[23] This interpretation was largely based upon the results of a previous electron diffraction study.[5] While their experimental results clearly reveal a radial structure in PPTA, the information obtained is on a different length scale from that reported in this study. For this reason, fiber scale crystallographic texture corresponding to the RFT model could not be observed. As well as this difference in the type of information provided, on-axis microdiffraction has several key advantages over other microscopy techniques for such studies. For example, the preparation of thin fiber cross sections for electron diffraction and optical microscopy is extremely difficult. Dobb et al. note the risk of distorting embedded samples during cutting while Hagege et al. report some folding of the ultrathin sections.[5,23] By contrast, the microdiffraction technique does not require particularly thin samples which makes embedded unnecessary.

3.2. Rotational Disorder. If the azimuthal maximum of a scattering profile represents the average orientation of crystal planes, then its azimuthal width (or HWHM) provides a direct measure of the degree of alignment. This can be explained in terms of an increase in the azimuthal angular width corresponding to an increase in the angular distribution of crystal planes illuminated by the X-ray beam. In this sense it can be considered as a measure of rotational disorder with respect to perfect orientation.

Although the general term "rotational disorder" is used in this study in reference to azimuthal broadening, there are actually two contributions which need to be considered. The first can be referred to as "direct" rotational disorder in the sense that it represents a distribution in the degree of preferred orientation (i.e., crystalline domains have a certain freedom to rotate about the fiber axis). This translates directly into a similar distribution over the azimuthal intensity profile for *hk*0 reflections. The second contribution is an indirect effect related to the distribution in axial domain orientation (i.e., a misorientation between [001] for crystalline domains and the fiber axis). This arises because the diffracting planes are not quite parallel to the fiber axis. In the Ewald construction this second contribution can be attributed to the fact that reciprocal lattice rotations normal to the [001]/[*hk*0] plane originate from a point which is not directly on the Ewald sphere's surface. Consequently, any distribution in domain orientation along this plane is projected onto the Ewald sphere's surface as an arc whose azimuthal width is dependent upon the degree of axial orientation. While both contributions will influence the azimuthal profiles observed on-axis, this latter effect will be relatively insignificant in the case of PBO due to its high degree of axial crystalline domain orientation. This is directly evident from the broad azimuthal profiles shown in Figure 4. This demonstrates that azimuthal broadening must be dominated by "direct" rotational disorder rather than the indirect influence of axial domain misorientaion.

Figure 7 shows an interpolated plot in which the azimuthal HWHM parameter calculated from each diffraction pattern is positioned according to the scan area. All HWHM values have been averaged between the 200 and 010/$\bar{2}$10 reflections in order to decrease fitting errors. As the angular relationships between (200), (010), and ($\bar{2}$10) crystal planes are fixed according to unit cell geometry, averaging can be justified. In addition, averaging is further supported by the similarity found in azimuthal HWHM between the two data series during model fitting. This latter point is in itself significant as the combined 010/$\bar{2}$10 reflection is expected to be azimuthally broader than that of the 200 reflection. This is partly due to the oblique angle (γ) of the PBO unit cell, but also because of the internal angle between [010] and [$\bar{2}$10]. As this difference in HWHM is not observed experimentally, PBO may have an idealized crystallographic structure in which (010) is slightly offset in its radial alignment about the fiber axis. However, as the 010/$\bar{2}$10 scattering profile is dominated by the 010 contribution (due to its shorter reciprocal scattering vector), this interpretation is entire speculative.

Figure 7 shows that the fiber exhibits a higher degree of rotational disorder at its center and edges. This is consistent with disordered core and skin regions, separated by a more ordered intermediate layer. A higher degree of rotational disorder in the fiber skin region is in general agreement with several previous studies. For example, Roth et al. include this feature in their model of rotational disorder in PPTA,[10] while other studies have reported the skin of PPTA to be almost amorphous.[2] A more disordered/misoriented fiber skin is also reported for the PBO fiber type, derived both from modeling[11] and direct observation.[12] Another interesting feature in Figure 7 is the variability in the skin's degree of rotational disorder and its changing thickness around the fiber's circumference. This observation has been predicted by PPTA fiber modeling which requires a skin of varying thickness to account for intensity variations across a single fiber.[10] In addition, differences in the degree of axial crystalline domain orientation are reported across the same PBO fiber width.[12] Such a result has important

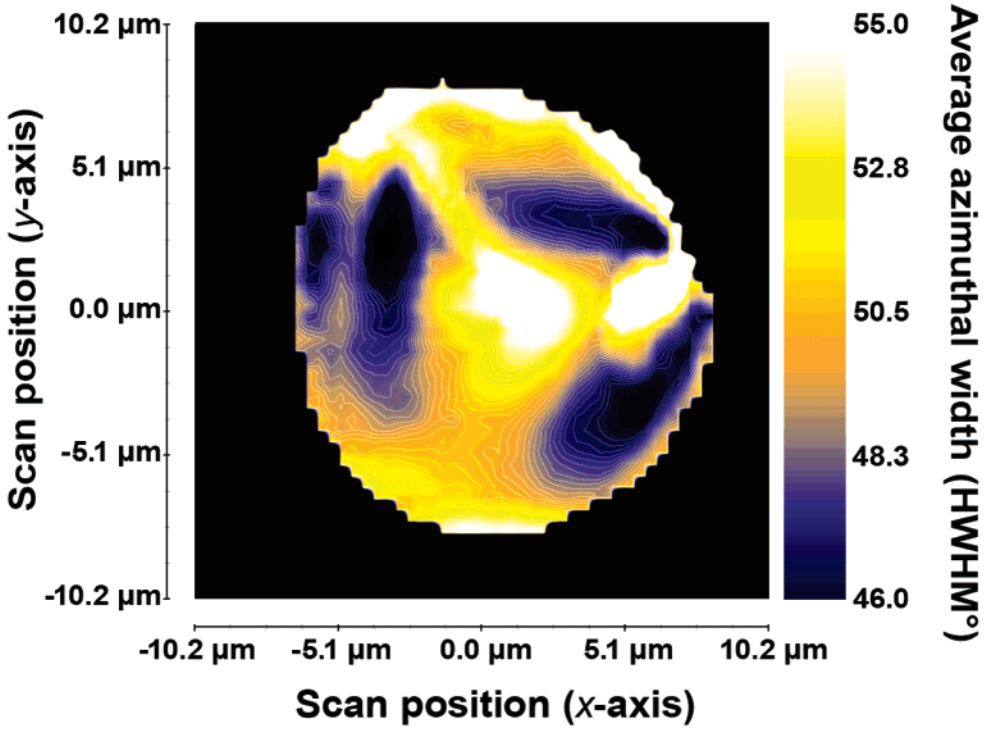

Figure 7. Interpolated area plot showing the average azimuthal HWHM calculated at each scan position on the fiber cross section.

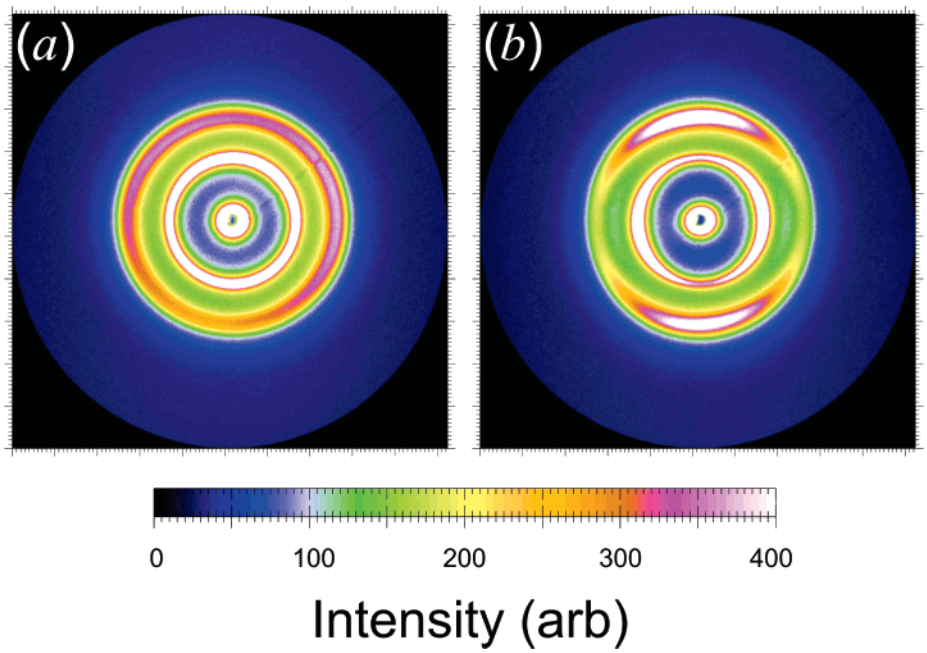

Figure 8. Comparison of diffraction patterns obtained (a) in fiber core region (representing a high HWHM) and (b) equidistant between the skin and core (representing a low HWHM).

implications for experimental techniques such as micro-Raman spectroscopy and AFM which are highly localized and surface sensitive.

The region around the geometric center of the fiber in Figure 7 can be designated the fiber core. In similarity with the fiber skin, this region also exhibits a higher degree of rotational disorder. Indeed, the degree of rotational disorder in the core is sufficiently high that scattering from both reflections becomes almost completely isotropic. This is shown in Figure 8 where one diffraction pattern obtained from the fiber core is compared against another collected from within the intermediate region. A more disordered or misoriented fiber core features in several existing structural models for both the PPTA and PBO fiber types.[10,11] It has also been inferred from μXRD studies performed using standard fiber diffraction geometry.[8,12] The fact that this feature can now be validated by direct on-axis observation and without the need for model assumptions is significant.

Another model-predicted feature which is confirmed experimentally in Figure 7 is core asymmetry. Indeed, not only is the core region slightly asymmetric, but it is also offset from the geometric fiber center. An off-center core has been previously observed from the electron microscopy of thin PPTA fiber sections (although in this case it was not mentioned within the study itself but is nevertheless apparent within the published micrographs).[23] It also features in several recent models for high-

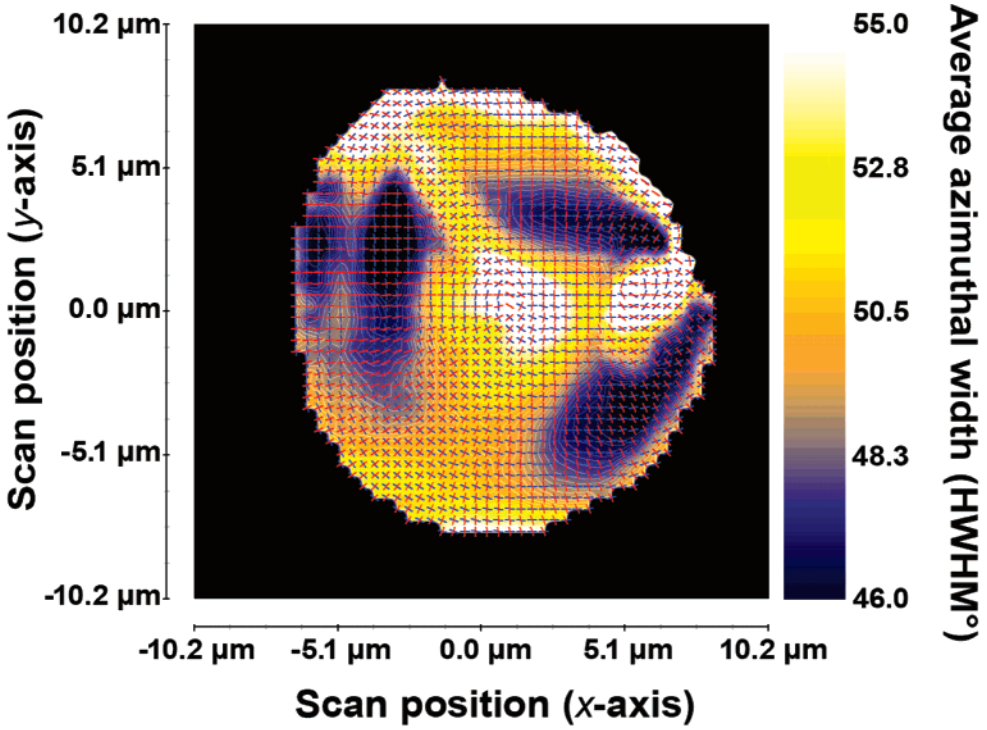

Figure 9. Relationship between rotational disorder and average local orientation for the (010) and (200) crystal planes (overplotted using red and blue lines, respectively).

performance fiber structure.[10,11] Roth et al. proposed this for PPTA fibers,[10] while a similar model is reported for the PBO fiber type.[11] Core asymmetry was also incorporated into this latter model,[11] a feature which can now be fully justified. The region of increased rotational disorder near to the center of the fiber is designated the fiber core due to its position and size. However, there is also a second region in Figure 7 which shares a similar structure but is offset by ~5 μm. On the basis of the structural similarity between these two regions (individual diffraction patterns at both positions show relatively isotropic scattering), this smaller region of increased rotational disorder can be interpreted as a secondary, smaller core-type feature.

3.3. Fiber Formation. The crystallographic texture and rotational disorder results reported in this study contain a number of interesting features. However, to discuss these features in greater detail requires an understanding of their structural origins. Although this fiber was not spun in situ, the experimental results nevertheless provide a number of clues from which these origins can be inferred. When coupled with the results of previous studies, it allows the process of fiber formation to be investigated, albeit indirectly. For example, it is possible to hypothesize that rotational disorder in the fiber skin occurs due to its rapid coagulation. This leaves little time for local reorganization, resulting in a lower degree of crystallinity and a higher level of disorder. The idea that disorder can be "frozen in" has been generically proposed in the PPTA model by Rao et al.[25] In addition, Ran et al. report that coagulation is initially limited to the fiber skin region and occurs within 300 ms.[26] Within the intermediate layer beyond the skin there is a lower degree of rotational disorder. This may reflect the coagulation rate being slowed by diffusion inside the fiber, allowing more time for local reorganization. This idea is in agreement with a study by Kitagawa et al. which reports a negative correlation between fiber homogeneity and coagulation rate.[27]

While the fiber skin region may have a higher degree of rotational disorder, it still exhibits preferred orientation with on-axis reflections which are azimuthally anisotropic. This is highly significant because there is considerable evidence in Figure 6 that preferred orientation develops throughout the fiber from the initial orientation within the fiber skin. For example, there is no specific point at the geometric center of the fiber from which a radial fiber texture appears to originate. Furthermore, crystal plane orientation seems to follow the fiber's local geometry most closely at its edge. These features are consistent with a preferred orientation which grows inward toward the center of the fiber. On the basis of Figure 6 and unit cell geometry, the skin region must form stacks of face-on PBO molecules during coagulation which are almost normal to the fiber's edge. This corresponds to initial molecular organization along the [010] direction of the PBO unit cell. Subsequent domain growth inside the fiber would correspond to organization along the [100] direction. With this in mind, this hypothesis is supported by a previous WAXS study of PBO coagulation.[26,28] Ran et al. report only the 010 reflection to appear during initial coagulation of the fiber skin. This is interpreted as molecular stacks forming containing face-on PBO molecules.[26,28] A delay is also reported in the appearance of the 200 reflection.[26,28] This would correspond to organization in the [100] direction which would be expected if diffusion causes the coagulation rate to slow following the skin's initial formation.[26]

After initial coagulation of the fiber skin, its radial arrangement of (010) crystal planes acts as a template from which crystallographic texture extends to the interior of the fiber. Thus, with a slowing coagulation rate due to diffusion, the existing crystalline domains grow toward the fiber core. At the same time as this crystallographic structure develops, the fiber's morphological structure of fibrils and microvoids forms due to the volume reduction following solvent removal. This has been demonstrated experimentally through the simultaneous appearance of WAXS and SAXS during PBO coagulation.[26] The fact that crystallographic and fibrillar structural development occurs simultaneously explains how local orientation is able to persist between adjacent fibrils. This cannot be readily explained if

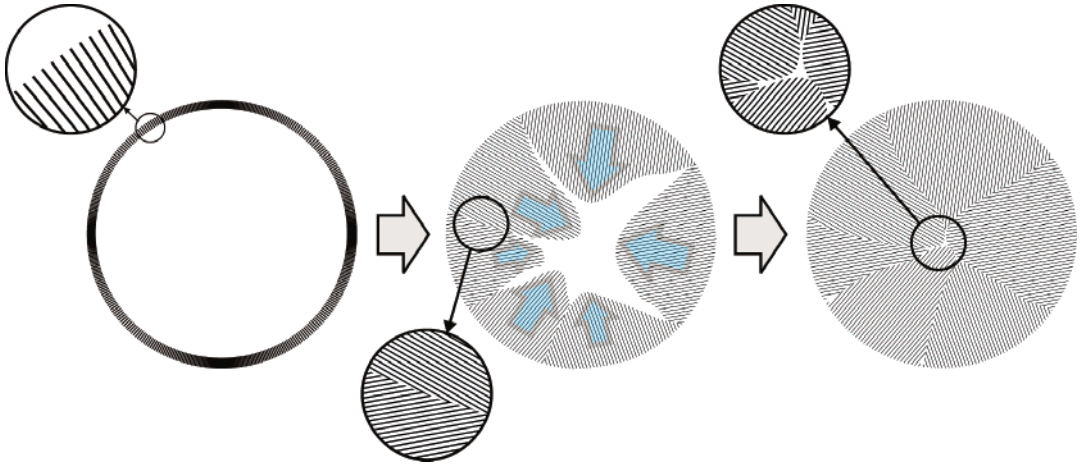

Figure 10. Schematic representation of an idealized PBO fiber formation model which can explain the fiber's internal structure observed experimentally.

domain boundaries form prior to coagulation, as has been proposed previously.[7]

A consequence of this model for crystallographic texture development should be the formation of extended domains sharing a common crystallographic orientation. Such features can be observed in Figure 6 as regions in which crystal plane orientation does not exhibit a constant angular rotation about the center of the fiber. Domain boundaries are also apparent where different crystallographic orientations converge. These are characterized by an increased azimuthal HWHM due to the simultaneous measurement of two different crystallographic orientations at the domain boundaries. To help clarify these features, Figure 9 shows the different elements from Figures 6 and 7 combined together into a single plot. The increased HWHM is clearly visible where different crystallographic orientations converge. It should be noted that the local points in Figure 9 at which average crystal plane orientations are no longer perpendicular reflect fitting inaccuracies. This occurs at points where the scattering pattern is almost isotropic and can therefore no longer be accurately fitted using Gaussian functions.

So far, fiber formation has only been discussed in terms of the skin region and its role in initiating a fiber-scale preferred orientation. However, the hypothesis of domain growth which explains crystallographic texture development can also explain the appearance of the fiber core. Figure 9 reveals that the core corresponds to the location at which multiple crystalline domains converge. However, unlike a domain boundary where two similar crystallographic orientations meet, the core region marks the convergence of multiple orientations. Thus, the increased azimuthal HWHM can be explained in terms of a number of crystallographic orientations simultaneously illuminated by the X-ray beam. In addition to this, it is also possible that local constraints to chain mobility contribute to the higher degree of rotational disorder in the core. This may be expected in the final stages of coagulation when the core region is already constrained by immobile material. A consequence of this hypothesis is that the position and shape of the fiber core will be defined by the location at which the converging domains meet and the manner of their intersection. An off-center or asymmetric core, as in Figure 9, may reflect heterogeneous coagulation and variations in the rate of domain growth. This hypothesis can also explain the rotationally disordered region, positioned $\sim 5\ \mu$m to the right of the main core. This secondary core is also located at the point at which multiple domains meet. This implies such features could occur wherever several domains intersect. In addition, skin−core morphology may vary significantly around a single fiber, similar to the reported variations in fiber diameter.[29]

The presented hypothesis for PBO fiber formation is shown schematically and idealized in Figure 10. The three main stages responsible for the development of the skin−core structures observed experimentally in this study are shown. These are (left) the rapid formation of a radially oriented fiber skin, (center) the inward growth of crystalline domains and the creation of domain boundaries, and (right) the development of a disordered core corresponding to the position of domain convergence.

4. Conclusions

The present study demonstrates the value of utilizing submicrometer X-ray beams for probing the crystallographic structure and microscopic morphology of high-performance fibers. The novel on-axis collection geometry provides a means of assessing various parameters which cannot be determined using the standard fiber diffraction geometry, many of which are also difficult to monitor using other experimental methods. This approach eliminates the need for model assumptions such as fiber symmetry, while providing spatially resolved information which does not require the extrapolation of individual measurements to bulk length scales. As a result, existing models of skin−core morphology can be quantitatively assessed and new features investigated.

The radial fibrillar texture model of fiber-scale crystallographic orientation is found to match the experimental results obtained for PBO. Thus, (010) crystal planes have an average alignment which is approximately radial about the fiber axis. It can be hypothesized that this radial crystallographic texture originates from local orientation in the fiber skin during coagulation. This forms a template for subsequent domain growth extending throughout the fiber. Variations in the angular distribution of crystal planes illuminated by the X-ray beam agree with this hypothesis. Where different orientations converge, domain boundaries can be identified by their increased degree of rotational disorder. The fiber's microvoid and fibrillar morphology evolves simultaneously with the development of preferred orientation. This explains how local crystallographic texture can persist between adjacent fibrils.

The skin−core structure of an as-spun PBO fiber consists of an intermediate layer positioned between more disordered skin and core regions. Rotational disorder in the fiber skin can be attributed to its rapid coagulation which limits structural reorganization. Meanwhile, the intermediate layer coagulates

at a slower rate due to diffusion effects in the coagulation bath. The disordered fiber core can be attributed to converging crystalline domains and limited chain mobility. The position and shape of the fiber core are therefore dictated by coagulation homogeneity. In this study, heterogeneous coagulation can explain variations in the thickness of the fiber skin and a core which is neither geometrically centered nor symmetrical. The existence of a second region sharing a similar structure to the fiber core suggests that multiple core-type features are possible within a single fiber.

Acknowledgment. The authors thank Toyobo (Japan) for supplying the PBO fiber samples used in this study. The assistance of the ID13 beamline support team is appreciated.

References and Notes

(1) Young, R. J.; Lu, D.; Day, R. J.; Knoff, W. F.; Harris, H. A. *J. Mater. Sci.* **1992**, *27*, 5431−5440.
(2) Graham, J. F.; McCague, C.; Warren, O. L.; Norton, P. R. *Polym. Commun.* **2000**, *41*, 4761−4764.
(3) Li, S. F. Y.; McGhie, A. J.; Tang, S. L. *Polymer* **1993**, *34*, 4573−4575.
(4) Kitagawa, T.; Yabuki, K.; Young, R. J. *J. Macromol. Sci., Phys.* **2002**, *B41*, 61−76.
(5) Dobb, M. G.; Johnson, D. J.; Saville, B. P. *J. Polym. Sci., Part B: Polym. Phys.* **1977**, *15*, 2201−2211.
(6) Muller, M.; Riekel, C.; Vuong, R.; Chanzy, H. *Polymer* **2000**, *41*, 2627−2632.
(7) Martin, D. C.; Thomas, E. L. *Macromolecules* **1991**, *24*, 2450−2460.
(8) Riekel, C.; Dieing, T.; Engstrom, P.; Vincze, L.; Martin, C.; Mahendrasingam, A. *Macromolecules* **1999**, *32*, 7859−7865.
(9) Riekel, C.; Cedola, A.; Heidelbach, F.; Wagner, K. *Macromolecules* **1997**, *30*, 1033.
(10) Roth, S.; Burghammer, M.; Janotta, A.; Riekel, C. *Macromolecules* **2003**, *36*, 1585−1593.
(11) Davies, R. J.; Burghammer, M.; Riekel, C. *Macromolecules* **2005**, *38*, 3364−3370.
(12) Davies, R. J.; Burghammer, M.; Riekel, C. *J. Synchrotron Radiat.* **2005**, *12*, 765−771.
(13) Riekel, C.; Davies, R. J. *Curr. Opin. Colloid Interface Sci.* **2005**, *9*, 396−403.
(14) Davies, R. J.; Montes-Moran, M. A.; Riekel, C.; Young, R. J. *J. Mater. Sci.* **2003**, *38*, 2105−2115.
(15) Davies, R. J. *J. Appl. Crystallogr.* **2006**, *39*, 262−266.
(16) Davies, R. J. *J. Appl. Crystallogr.* **2006**, *39*, 267−272.
(17) Kitagawa, T.; Murase, H.; Yabuki, K. *J. Polym. Sci., Part B: Polym. Phys.* **1998**, *36*, 39−48.
(18) Davies, R. J.; Montes-Moran, M. A.; Riekel, C.; Young, R. J. *J. Mater. Sci.* **2001**, *36*, 3079−3087.
(19) Hammersley, A. P.; Svensson, S. O.; Thompson, A. *Nucl. Instrum. Methods Phys.* **1994**, *346*, 312−321.
(20) Fratini, A. V.; Lenhert, P. G.; Resch, T. J.; Adams, W. W. *Mater. Res. Symp. Proc.* **1989**, *134*, 431.
(21) Kitagawa, T.; Murase, H.; Yabuki, K. *J. Polym. Sci., Part B: Polym. Phys.* **1998**, *36*, 39−48.
(22) Krause, S. J.; Haddock, T. B.; Vezie, D. L.; Lenhert, P. G.; Hwang, W.-F.; Price, G. E.; Helminiak, T. E.; O'Brien, J. F.; Adams, W. W. *Polymer* **1988**, *29*, 1354−1364.
(23) Hagege, R.; Jarrin, M.; Sotton, M. *J. Microsc.* **1979**, *115*, 65−72.
(24) Jacquemart, J.; Hagege, R. *J. Microsc. Spectrosc. Electron.* **1978**, *3*, 427−438.
(25) Rao, Y.; Waddon, A. J.; Farris, R. J. *Polymer* **2001**, *42*, 5937−5946.
(26) Ran, S.; Burger, C.; Fang, D.; Zong, X.; Cruz, S.; Chu, B.; Hsiao, B. S.; Bubeck, R.; Yabuki, K.; Teramoto, Y.; Martin, D. C.; Johnson, M. A.; Cunniff, P. M. *Macromolecules* **2002**, *35*, 433−439.
(27) Kitagawa, T.; Ishitobi, M.; Yabuki, K. *J. Polym. Sci., Part B: Polym. Phys.* **2000**, *38*, 1605−1611.
(28) Ran, S.; Burger, C.; Fang, D.; Zong, X.; Chu, B.; Hsiao, B. S.; Ohta, Y.; Yabuki, K.; Cunniff, P. M. *Macromolecules* **2002**, *35*, 9851−9853.
(29) Hunsaker, M. E.; Price, G. E.; Bai, S. J. *Polymer* **1992**, *33*, 2128−2135.

MA062049G